Title: Early detection of human glioma sphere xenografts in mouse brain using diffusion MRI at 14.1 T.

Authors: Porcari P, Hegi ME, Lei H, Hamou MF, Vassallo I, Capuani S, Gruetter R, Mlynarik V

Journal: NMR in biomedicine

Year: 2016 Nov

Volume: 29

Issue: 11

Pages: 1577-1589

DOI: 10.1002/nbm.3610

Early detection of human glioma sphere xenografts in mouse brain using diffusion MRI at 14.1 Tesla

Short title: Early detection of glioma xenografts using diffusion MRI at 14.1T

P. Porcari[a,b*], M. E. Hegi[c], H. Lei[a,d], MF. Hamou[c], I. Vassallo[c], S. Capuani[e], R. Gruetter[a,d,f,g], and V. Mlynarik[a,h]

**Correspondence to*: *P. Porcari, Newcastle Magnetic Resonance Centre, Newcastle University, Newcastle Upon Tyne, UK. E-mail: paola.porcari@ncl.ac.uk*

a *P. Porcari, H. Lei, R. Gruetter, V. Mlynarik*

Centre for Biomedical Imaging, Ecole Polytechnique Fédérale de Lausanne, Lausanne, Switzerland

b *P. Porcari*

Newcastle Magnetic Resonance Centre, Newcastle University, Newcastle Upon Tyne, UK

c *M.E. Hegi, M.-F. Hamou, I. Vassallo*

Laboratory of Brain Tumor Biology and Genetics, Service of Neurosurgery and Neuroscience Research Centre, Department of Clinical Neurosciences, Lausanne University Hospital and University of Lausanne, Lausanne, Switzerland

d *H. Lei, R. Gruetter*

Department of Radiology, University of Geneva (UNIGE), Geneva, Switzerland

e *S. Capuani*

CNR-ISC UOS Roma Sapienza, Physics Department, Sapienza University of Rome, Rome, Italy

f *R. Gruetter*

Department of Radiology, University of Lausanne, Lausanne, Switzerland

g *R. Gruetter*

LIFMET, *Ecole Polytechnique Fédérale de Lausanne, Lausanne, Switzerland*

h *V. Mlynarik*

High Field MR Center, Medical University of Vienna, Vienna, Austria

Abstract

Glioma models have provided important insights into human brain cancers. Among investigating tools, magnetic resonance imaging (MRI) has allowed their characterization and diagnosis.

In this study, we investigated whether diffusion MRI might be a useful technique for early detection and characterization of slow-growing and diffuse infiltrative gliomas, such as the proposed new models, LN-2669GS and LN-2540GS glioma sphere xenografts. Tumours grown in these models are not visible in conventional T_2-weighted and contrast-enhanced T_1-weighted MRI at 14.1T.

Diffusion weighted imaging (DWI) and diffusion tensor imaging (DTI) protocols were optimized for contrast by exploring long diffusion times sensitive for probing the microstructural alterations induced in the normal brain by the slow infiltration of glioma sphere cells.

Compared with T_2-weighted images, tumours were properly identified in their early stage of growth using diffusion MRI, and confirmed by localized proton MR spectroscopy as well as immunohistochemistry. The first evidence of tumour presence was revealed for both glioma sphere xenograft models three months after tumour implantation, while no necrosis, oedema or haemorrhage were detected either by MRI or by histology. Moreover, different values of diffusion indices, such as mean diffusivity (MD) and fractional anisotropy (FA), were obtained in tumours grown from LN-2669GS and LN-2540GS glioma sphere lines, respectively. These observations highlighted diverse tumour microstructures for both xenograft models, which were reflected in histology.

This study demonstrates the ability of diffusion MRI techniques to identify and investigate early stages of slow-growing, invasive tumours in the mouse brain, thus providing a potential imaging biomarker for early detection of tumours in humans.

Keywords: diffusion MRI, ADC, MD, FA, brain tumours, human glioma xenografts, MRS, immunohistochemistry

Abbreviations used: *ADC, apparent diffusion coefficient; δ, gradient-pulse-duration; Δ, gradient-pulses-separation, diffusion time; DAB, diaminobenzidine tetrahydrochloride; DTI, diffusion tensor imaging; DWI, diffusion weighted imaging; FA, fractional anisotropy; FASTMAP, fast automatic shimming techniques by mapping along projections, GBM, glioblastoma multiforme; GFAP, glial fibrillary acidic protein; GIC, glioma-initiating cells; Glc, Glucose; Gln, Glutamine; Gly, glycine; Glu, Glutamate*; *Ins, myo-inositol;* $l = (2D\Delta)^{1/2}$, *diffusion distance; MAB, monoclonal antibody; MD, mean diffusivity; MIB-1, mindbomb E3 ubiquitin protein ligase 1; NAA, N-acetyl-aspertate; NAAG, N-acetylaspartylglutamate; NCL, nucleolin; PGSTE, pulse gradient stimulated echo; ROI, region of interest; SPECIAL, spin echo, full intensity acquired localized; Tau, taurine; tCho, total choline; tCr, total creatine; TP53, tumour protein 53; VAPOR, variable power and optimized relaxation; VOI, volume of interest.*

INTRODUCTION

Diffuse gliomas (WHO grade II to IV) (1) are the most common primary brain tumours in humans and one of the leading causes of cancer-related deaths in adults (2). Their diffuse infiltration into the surrounding normal brain precludes complete resection and they all eventually recur, usually having progressed to a more aggressive tumour. The infiltrative part will give rise to tumour recurrence even in MRI-controlled, macroscopically fully resected patients, since the extent of invasion is not visible using conventional T_1 and T_2-weighted MRI. Hence, it is difficult to target treatment to this "invisible" part. Among diffuse gliomas, glioblastoma (GBM, World Health Organization [WHO] grade IV) is the most aggressive form (3) with a median overall survival of only 14.6 months (4) despite multimodal treatment of maximal safe resection, followed by combined chemo-radiotherapy. Visualization of the infiltrative portion of gliomas is a necessary first step for testing novel treatment strategies affecting migrating tumour cells (5).

Over the past decades, rodent models of diffuse infiltrative gliomas have been extensively investigated (6-8) to better understand the genetic and molecular pathology of malignant gliomas and to assess the efficacy of newer therapies (9). Although none of the existing models fully reflect the corresponding human neoplasm (7), their use in combination with advanced neuroimaging techniques (10-12) has led to the identification of imaging biomarkers for the detection of brain cancers and early prediction of therapeutic efficacy (13).

MRI allows non-invasive *in vivo* monitoring of both tumour growth and response to therapy, and provides detailed structural information on tumour and brain tissue (14). Morphological features of diffuse gliomas, e.g. tumour location and size, necrosis, peritumoral oedema, heterogeneity, and haemorrhagic foci can be determined using routine contrast-enhanced T_1-, and T_2-weighted MRI. Nevertheless, conventional MRI has limited sensitivity and specificity in evaluating early therapeutic effects, in determining histological type and tumour grading and in accurately delineating tumour extent (15). Contrast-enhanced T_1-weighted MRI tends to underestimate the diffuse infiltration of glioma cells (16) depending on the blood-brain-barrier

integrity at the infiltrative margins (17). In addition, histological correlation with T_2-weighted images of gliomas has shown glioma-infiltrating cells beyond the hyper-intense region on T_2-weighted images (18).

To overcome these limitations, advanced MRI methods sensitive to tissue properties related to brain cancer biology and glioma cell migration have been developed and implemented (14,19). Among these, diffusion MRI (20), which reflects information on the tissues microstructure, potentially allows imaging of glioma-infiltrating cells in the normal brain (21) and the detection of early changes in the tumour microenvironment following treatment (22). The diffusion-weighted MR signal, which is recorded as a function of diffusion weighting or *b*-value, is affected by the complex composition and the geometric architecture of the investigated tissues. Due to the presence of structural barriers, water diffusion in brain tissue is restricted and/or hindered. Therefore, the diffusion time (Δ) becomes a key parameter for improving the sensitivity of diffusion MRI to tissue microstructure. For longer Δ, water molecules in the brain probe more obstacles and/or barriers over larger spatial scales, which are, however, smaller than the dimensions of a pixel. Moreover, with increasing Δ diffusion can be considered "quasi-Gaussian" in normal physiological condition and the measured diffusion coefficient shows a rather monotonic behaviour as function of Δ and membrane permeability (23), which is more visible for shorter diffusion times (24). Therefore, the measured diffusion coefficient, which reflects tissue characteristics, might change with the tumour progression for longer Δ thus playing an important role to evaluate healthy and diseased tissues. To our knowledge, no previous studies have reported the effect of Δ on water diffusion in human glioma models, except an *in vitro* study on glioma cells (25). By increasing the diffusion time, water molecules probe a wider area of tissue in accordance to the relation ($l = (2D\Delta)^{1/2}$) between the diffusion distance (l) and the diffusion time (Δ). As a consequence, we hypothesise that the diffusion signal at extended Δ will be more sensitive to the small changes in cell density which are characteristic of the slow infiltration of gliomas. This feature is well modelled in the investigated xenografts.

Currently, DWI (27) and DTI (28-29) techniques are commonly used to investigate diffuse infiltrative gliomas in both preclinical (30-31) and clinical settings (32-33). These techniques allow the detection of the invasive pathways of glioma cell migration in the brain, which seem to preferentially occur along the myelinated fibres in white matter tracts (1,34).

Using optimized diffusion protocols at 14.1T, the aim of this study was to identify slow-growing glioma sphere xenografts in their early stages of growth, which are otherwise not visible using conventional Gd-DTPA enhanced T_1-weighted (36) and T_2-weighted MRI. In addition, differences in diffusion indices of LN-2669GS and LN-2540GS glioma sphere xenografts allowed the evaluation of differences in their microstructure. Tumour growth detected by diffusion methods was confirmed by localized proton MR spectroscopy (MRS) and immunohistochemistry.

MATERIALS AND METHODS

Glioma-derived sphere lines

Two human glioma-derived sphere lines, LN-2540GS and LN-2669GS (35,36), were used for orthotopic xenografts in nude mice. As previously described (35), each line was derived by mechanical and enzymatic dissociations of GBM surgical specimens into a single cell suspension. After CD133 (Miltenyi Biotec) selection procedure, cells were cultured under stem cell conditions in DMEM-F12 medium (Invitrogen; 10565-018) supplemented with 2% of B27 (Invitrogen; 17504), human recombinant epidermal growth factor (20 ng/mL) and human recombinant basic fibroblast growth factor (20 ng/mL) (Peprotech; AF-100-15 and 100-18B).

Basic genetic characterization and authentication have been published previously (35,36).

Animal Model

Orthotopic human gliomas were induced in eight female athymic nude mice (Swiss nu/nu; Charles River France, France), aged 6-9 weeks and weighing 20-28g. All experimental procedures and animal care were performed according to the federal and local ethical guidelines and approved by the local veterinary authorities (VD 1181-5). Mice were anesthetized and placed into a stereotaxic frame (Stoelting Co., Wood Dale, IL, USA). Glioma sphere cells

(1×10^5), dissociated into a single cell suspension, were injected in a volume of 5 µl of PBS via a stereotaxic injector at a flow rate of 5 µl/min (Quintessential Stereotaxic Injector (QSI)^{TM}) into the right striatum of the mice (coordinates from bregma: 0.0 mm posterior, 2.5 mm lateral, 3.0 mm ventral; n=4 per sphere line).

Animal preparation for MRI

Fifty days after orthotopic implantation of human glioma sphere cells, mice underwent MRI for the first time and then once a week. Control mice (n=4) were also investigated using the same MRI protocol.

For MRI measurements, each mouse was anaesthetized with isoflurane (4% induction, 1.5-2% maintenance) in a mixture of air:O_2 (1:0.5 l/min induction, 0.7/0.3 l/min maintenance), and placed in a home-built dedicated holder with the head stereotaxically fixed by ear pins and bite bar. Physiological monitoring was performed using an MRI-compatible small animal monitoring and gating system (Model 1025, SA Instruments, Stony Brook, NY, USA). The body temperature was maintained in the range 36.5 - 37.5 °C using a circulating warm water system and the respiratory rate kept between 60 and 90 bpm by regulating the isoflurane level.

MR imaging

All measurements were performed on a 14.1 T/26 cm horizontal bore magnet (Magnex Scientific, Oxford, UK) interfaced to a Direct Drive console (Varian Medical System, Palo Alto, CA, USA), and equipped with a 12-cm inner diameter actively-shielded gradient set (400 mT/m in 120 µs). A two-loop quadrature surface coil was used as a radio-frequency transceiver for MR imaging and spectroscopy. MRI protocol included T_2-weighted images, DWI and DTI scans. After measuring scout scans, multi-slice T_2-weighted fast spin-echo (TSE) images of mouse brain were acquired in the coronal orientation as an anatomical reference (TR/TE_{eff} = 5000/52 ms, echo train length = 8, field-of-view = 20 × 20 mm^2, matrix size = 256 × 256, in-plane resolution of 78 × 78 μm^2, 13 slices of 0.6 thickness, 4 averages, scan time of 10 min). Static field homogeneity was optimized by adjusting all first and second order shims using an

EPI version of FASTMAP (37), resulting in water linewidths of 18-24 Hz over the selected volume of interest ($6 \times 5 \times 4.5$ mm^3) centered in the mouse brain.

Diffusion-weighted images of mouse brain were acquired in the coronal orientation using a pulse gradient stimulated echo (PGSTE) sequence (38) (TR/TE = 4000/22 ms; field-of-view = 20×10 mm^2, matrix size = 128×64, in-plane resolution = 156×156 μm^2, 8 slices of 1 mm thickness sufficient to cover the whole tumour and the peritumoral areas, 2 averages, scan time of 67 min).

To optimize DWI and DTI protocol for glioma detection, a pilot study was carried out on mice with LN-2540GS xenograft at early stages of tumour development by exploring several diffusion times (Δ = 40, 60, 80, 100, 150, 220 ms) with gradient duration (δ) equal to 4ms. For each Δ, DWI data were acquired using eight *b*-values (294, 389, 542, 754, 1024, 1352, 2185, 2688 s/mm^2) with the diffusion gradient applied along the readout direction (X-axis). The corresponding gradient amplitudes are summarized in Table 1. It is of note that the calculation of *b*-values includes the contribution of imaging and crusher gradients which lead to *b*0-values for the un-weighted diffusion images, as reported in Table 1. Contrast-to-noise ratio (CNR) of tumour was calculated for each DW image (acquired at each specified Δ and *b*-value) as the difference between the mean signal from regions-of-interest (ROIs) drawn (as circular areas of the same size) in the contralateral (CL) area, <CL>, and in the tumour (T), <T>, divided by the standard deviation of the signal in the CL region, σ(CL), [CNR = (<CL>-<T>)/ σ(CL)] (Table 2). Signal-to-noise ratio (SNR) of tumour was determined for each Δ on the b_0 image as the mean signal intensity of a ROI drawn in the tumour location (<T>) divided by the standard deviation (σ) of a large ROI in the background noise (N), that was visually devoid of artefacts [SNR = <T>/σ(N)].

Following the observation in this pilot study, the main DWI protocol for both glioma sphere derived xenografts, LN-2669GS and LN-2540GS, used Δ = 80ms with all the above-specified *b*-values, which was justified by the pilot study CNR data (Table 2, Fig.1). The same DWI

protocol was also carried out with diffusion gradients applied along the phase encoding (Y-axis) and the slice selection (Z-axis) directions.

CNR of tumour growing from both glioma sphere xenografts was also determined for $\Delta = 80$ ms as function of *b*-values for the DWI data acquired during the last MRI session.

DTI data were collected by acquiring seven images, one b_0 image (no diffusion weighted, b = 0 s/mm^2) and six diffusion-weighted images, each of them with the same *b*-value of 1352 s/mm^2, (which was found to provide the best tumour contrast by exploring different Δ and *b*-values in DWI scans as shown in Table 2) and encoding gradients applied in six unique orientations ([1,0,0], [0,1,0], [0,0,1], [$1/\sqrt{2}$,$1/\sqrt{2}$,0], [$1/\sqrt{2}$,0,$1/\sqrt{2}$], [0,$1/\sqrt{2}$,$1/\sqrt{2}$]). The acquisition time was 58 min.

Apparent diffusion coefficient (ADC) maps of mouse brain were computed by fitting, voxel-by-voxel, the signal intensity of the diffusion-weighted images as a function of *b*-values ($S(b) = S(0) \exp(-b \cdot ADC)$).

Diffusion tensor maps, MD and FA maps, which reflect respectively the average diffusivity and the degree of anisotropy in each voxel (27), were computed by reconstructing the tensor. All diffusion maps, ADC, MD and FA, were computed using FSL DTIFIT routine (FSL, version 4 software; http://www.fmrib.ox.ac.uk/fsl).

ROIs containing the tumour, a CL area, and the corresponding brain regions of controls were drawn (as circular areas of the same size) on the ADC, MD and FA maps with reference to the diffusion-weighted image with $\Delta = 80$ms, b = 1352 s/mm^2, where tumour showed better contrast (Table 2). The CL area was selected considering the brain region symmetric to the tumour location with respect to the mid-sagittal plane. Mean values of ADC, MD and FA were calculated in the selected ROIs using a custom Matlab script.

Statistically significant difference between the mean values of diffusion indices calculated in the selected ROIs of all tumour slices in all mice and in the corresponding CL was accepted for $P < 0.05$, as determined with a two-tailed, paired Student's t-test. Comparison between the diffusion

indices calculated in the tumour of both xenografts as well as the comparison between the diffusion indices calculated in the tumour of each xenograft and in the corresponding brain region of the control group were considered as statistically significant for $P < 0.05$, as determined with a two-tailed, unpaired Student's t-test.

MR spectroscopy

Spectra of gliomas were acquired during the final MRI session in each mouse. Proton spectra were collected using a short echo-time (TE = 2.8 ms) spin echo, full intensity acquired localized (SPECIAL) (39) spectroscopy sequence from a VOI ($2 \times 2 \times 2$ mm^3) located within the tumour, based on coronal diffusion-weighted images. Before measurements, field homogeneity was adjusted in the selected VOI, as mentioned above. Outer volume suppression interleaved with a VAPOR (variable power and optimized relaxation delays) (40) water signal suppression was used. Spectra were acquired with TR = 4000 ms, 15 blocks of 16 transients (total scan time 16 min), spectral width of 7 kHz using 4096 data points. Each block was corrected for static field drift and summed for further analysis. Spectra from brain regions of healthy mice matching tumour size and location in the brain of injected mice were acquired for comparison.

Metabolite concentrations were quantified by LCModel (41) and absolute concentration of metabolites were calculated using an unsuppressed water peak as a reference.

Statistically significant levels were accepted for $P<0.05$, as determined with a two-way ANOVA followed by the Bonferroni multi-comparison post-tests.

Immunohistochemistry

All mice were sacrificed approximately 5 months after implantation, when gliomas were sufficiently large (maximum dimension of 2 - 3 mm) in DW images. Brains were dissected, fixed in formalin (4% buffered formalin) and embedded in paraffin. Tissue sections (5 μm) were stained with H&E (hematoxylin and eosin) or immunostained for the following proteins: GFAP (glial fibrillary acidic protein; G3893, Sigma), MIB-1 (MAB, DAKO M7240), p53 (MAB, DAKO, M7001) (37), using standard procedures (VENTANA), and human nucleolin (hNCL, 1:200, 4°C, overnight; ab13541, abcam; does not react with mouse). For hNCL, the antigen

retrieval procedure in citrate phosphate buffer (pH 6.0) was performed at 95°C for 60 min followed by 8 min at 120°C (pressure cooker) and an additional blocking step of 15 min with Rodent Block M (cat # RBM 961, Biocare Medicale, Concorde, CA, USA) was added to the standard procedure. Immunoreactivity was visualized using DAB (diaminobenzidine tetrahydrochloride).

RESULTS

MRI results

The diffusion time Δ = 80 ms was found to be optimal for identifying the glioma sphere xenografts as shown from the pilot study CNR data (Table 2, Fig. 1). The extension of the lesions was not properly visualised using lower diffusion times whereas higher Δ led to unacceptably low SNR.

Tumours grown as LN-2669GS and LN-2540GS glioma sphere xenografts in mouse brain were detected for the first time three months after glioma implantation as shown in Fig. 2 and Fig. 3, respectively. Each of both figures shows typical T_2-weighted and diffusion-weighted images (Fig. 2a, b and Fig. 3a, b) acquired three months after cell injection and the calculated ADC, and DTI maps (Fig. 2c-f, Fig. 3c-f) of a coronal slice from the mouse brain with LN-2669GS NCH-1364 and LN-2540GS NCH-1365 glioma sphere xenograft, respectively.

In both figures, the hypo-intense region on the diffusion-weighted images (Fig. 2b, 3b), which is just visible for the LN-2669GS NCH-1364 xenograft (Fig. 2b), and the corresponding hyper-intense area on the ADC and MD maps (Fig. 2c-d, Fig. 3c-d) as well as the hypo-intense region on the FA map (Fig. 2e, Fig. 3e) shows the extent of the tumour. In contrast, no lesion is visible on the T_2-weighted images (Fig. 2a, Fig. 3a).

Fig. 4 and Fig. 5 show coronal T_2-weighted and diffusion-weighted images (Fig. 4a, b and Fig. 5a, b) acquired five months after injection of the cells as well as the computed ADC and DTI maps (Fig. 4c-f, Fig. 5c-f) from the mouse brain of the same mice displayed in Fig. 2 and Fig. 3, respectively. As with Fig. 2 and Fig. 3, both xenografts are visible in the diffusion-weighted images (Fig. 4b, Fig. 5b) as well as in the ADC (Fig. 4c, Fig. 5c) and DTI maps (Fig. 4d-f, Fig.

5d-f) whereas no evidence of tumour is seen in the corresponding T_2-weighted image (Fig. 4a, Fig. 5a).

Compared to Fig. 2 and Fig. 3, tumours grown from both sphere lines are more visible in Fig. 4 and Fig. 5, at five months after cell injection due to tumour development.

Fig. 6 shows DWI acquisition on the mouse brain comprising the LN-2540GS xenograft NCH-1365 (A) as well as the CNR data for both xenografts (B). All data were acquired during the last MRI session.

The progression of diffusion-weighted images (Fig. 6A, a-h), acquired two weeks after those presented in Fig. 5, demonstrates an improved delineation of tumour margins when the *b*-value increases. In particular, the lesion becomes visible when *b* is higher than 500 s/mm^2 (Fig.6A, c) and the higher the *b*-value, the more noticeable the tumour (Fig. 6A, c-h), which appears as a hypo-intense lesion on the diffusion-weighted images (Fig. 6A, c-h) and as a hyper-intense area in the corresponding ADC map (Fig. 6A, k). Conversely, the lesion is not visible on the T_2-weighted image (Fig. 6A, j) that shows only a ventricular enlargement, as in Fig. 5a.

The CNR data shown in Fig. 6B are displayed as a function of *b*-values (Δ = 80ms) for images acquired in the last MRI session (Fig. 4 and Fig. 6A, respectively). The best tumour contrast is given for both xenografts at a *b*-value equal 1352 s/mm^2, the same given by the pilot study CNR data (Table 2).

Mean values of the diffusion indices calculated in the tumour (T) and in the corresponding contralateral (CL) area of each xenograft as well as in the same brain regions of controls are summarized in Table 3 and Table 4 for both xenografts at early stages of tumour development (three months after injection) and at five months after cell injection, respectively.

For both stages of tumour growth, either three months or five months after cell injection (Table 3 and Table 4, respectively), a significant increase in MD was observed in tumours grown as LN-2669GS xenografts than in those grown from LN-2540GS cells compared to the CL area and to the values obtained from the same brain regions of controls. On the other hand, a significant decrease in FA was observed in both cases (Table 3 and Table 4) in tumours grown

as LN-2669GS xenograft whereas no changes were observed in those grown from LN-2540GS cells compared with the CL area and the control. Moreover, ADC values increased similarly in tumours grown from each xenograft (LN-2669GS or LN-2540GS xenografts), either at three or five months after cell injection (Table 3 and Table 4, respectively), compared with those in the contralateral area and in the controls.

By comparing the corresponding values of the diffusion indices for each stage of tumour development, either three months (Table 3) or five months after cell injection (Table 4), the diffusion indices are slightly lower at earlier stages of tumour growth (Table 3). However, no significant difference was found between each corresponding diffusion indices in the two investigated stages of tumour development.

MR Spectroscopic results

Proton spectra were measured immediately before sacrificing mice for histological assessment. In Fig. 7, ^{1}H spectra of a mouse brain from a control (Fig. 7a), LN-2669GS xenograft NCH-1364 (Fig. 7b) and LN-2540GS xenograft NCH-1365 (Fig. 7c) are shown.

The spectra of tumours (Fig. 7b - c) were acquired 5 months after injection of glioma sphere cells and compared with the control spectrum (Fig. 7a). The main changes in metabolite concentrations (indicated by arrows) are depicted in Fig. 7 and Fig. 8.

In particular, the tumour grown from the LN-2669GS sphere line (Fig. 7b) showed a decrease in NAA (4.7 μmol/g vs. 7.7±0.4μmol/g in controls, $p<0.01$), Glu (4.7 μmol/g vs. 8.4±0.4μmol/g, $p<0.001$), NAA+NAAG (5.7 μmol/g vs. 8.6±0.4μmol/g, $p<0.01$) and Glu+Gln (8.2 μmol/g vs. 10.8±0.4μmol/g, $p<0.05$) concentrations and an increase in Ins (10.8 μmol/g vs. 4.3±0.4μmol/g $p<0.0001$) and Glc (4.7 μmol/g vs. 1.5±0.3μmol/g, $p<0.01$) ones (solid black bars, Fig. 8).

The tumour grown from the LN-2540GS sphere line (Fig. 7c) showed a more profound reduction in NAA (1.8 μmol/g vs. 7.7±0.4μmol/g in controls, $p<0.0001$), Glu (3.7 μmol/g vs. 8.4±0.4μmol/g, $p<0.0001$), NAA+NAAG (2.6 μmol/g vs. 8.6±0.4μmol/g, $p<0.0001$) and Glu+Gln (6.2 μmol/g vs. 10.8±0.4μmol/g, $p<0.0001$) concentrations and an increase in the Ins

(15.0 μmol/g vs. 4.3±0.4μmol/g $p<0.0001$) and Glc (6.4 μmol/g vs. 1.5±0.3μmol/g, $p<0.0001$) with additional changes in Gly (5.0 μmol/g vs. 1.2±0.1μmol/g, $p<0.001$) and Tau (5.7 μmol/g vs. 12.6±1.1 μmol/g, $p<0.0001$), when compared to the LN-2669GS sphere line (solid gray bars, Fig. 8).

Immunohistochemical results

In order to assess imaging and spectroscopic results, histological and immunohistochemical analysis was performed on each mouse. Due to the highly invasive nature of the human LN-2669GS cells, the intracerebral lesion was not visible on the H&E section (Fig. 9a). The human nucleolin (NCL) immunostaining (Fig. 9c - d) identifies the human tumour cells, and visualizes the infiltrative growth pattern of the human LN-2669GS tumour cells. GFAP expression indicated a region with enhanced gliosis that reached over to the co-lateral side probably induced by tumour cell infiltration (Fig. 9b). The area with strongest gliosis, as indicated by GFAP expression, shown in Fig. 9b, correlates with the hypo-intense region in the diffusion-weighted image (Fig. 4b), the hyper-intense areas in the ADC and MD maps (Fig. 4c - d) and the hypo-intense regions in the FA map (Fig. 4e). Images shown in Fig. 4 as well as the spectrum displayed in Fig. 7b were all acquired during the last MRI session, immediately before euthanizing the mouse.

The LN-2540GS xenograft comprises a compact and a more invasive component visualized on the H&E (Fig. 9e) and the GFAP immunostained (Fig. 9f) coronal section as well as by the nuclear expression of TP53 (not shown), which is detected in all tumour cells in agreement with hNCL staining (Fig. 9g). The high cell density in the compact tumour area is visualized in Fig. 9g. The tumour area visible in Fig. 9e – g correlates with the hypo-intense regions visible on the DWI acquisition (Fig. 6c – h) and the hyper-intense area shown in Fig. 6k. Images shown in Fig. 6A and the spectrum reported in Fig. 7c were all acquired during the last MRI session, immediately before the mice were euthanized.

It is of note, the two xenografts display a striking difference in cell density, as visualized in Fig. 9d and Fig. 9h, displaying at high magnification an area of human tumour cells (with the same magnification): LN-2669GS xenograft (Fig. 9d) shows a lower tumour cell density than LN-2540GS xenograft (Fig. 9B, d).

In addition, none of the histological sections of both xenografts shows any areas of necrosis, in accordance with imaging results.

Discussion

We have developed a diffusion MR protocol at 14.1T for early detection and investigation of human glioma xenografts in mice. Its performance was documented on human glioma xenografts derived from the sphere lines LN-2540GS and LN-2669GS, characterized by their slow and diffuse infiltrative growth in the mouse brain (8). With the optimized acquisition parameters of the diffusion-weighted stimulated-echo (PGSTE) sequence, in particular the diffusion time (Δ = 80 ms), the protocol allowed a proper detection and investigation of both xenograft models in the regime of hindered diffusion.

Different diffusion times (Δ = 40-220ms) were explored in a pilot study carried out on LN-2540GS glioma sphere xenografts at early stages of growth and the best tumour contrast was found for Δ = 80ms (Table 2). By selecting this observation time, the diffusion distance ($l \sim 10$ µm) was comparable with the average distance between glioma sphere cells, which were not densely packed within the investigated xenografts due to their diffuse infiltrative growth. Therefore, shorter Δ do not give a proper tumour contrast whereas Δ = 80ms, by probing the distance between glioma sphere cells, optimizes tumour contrast for the investigated xenografts.

Different diffusion properties due to diverse tumour microstructure in each model were also demonstrated by the calculated diffusion indices. Finally, presence of the tumours was confirmed by localized spectroscopy and by immunohistochemical analysis, which also provided information on morphologic tumour properties.

As it is well known (38), the advantage of the PGSTE sequence is the use of long diffusion times avoiding signal loss due to the transverse relaxation time T_2. On the other hand, its main

disadvantage is a loss of 50 % of the MR signal (42). We partly compensated this loss by using the shortest possible TE (22 ms), an ultra-high magnetic field and a small surface coil (dimensions of 21mm x 14 mm). However, the increase in SNR due to the high magnetic field was reduced by shorter transverse relaxation time T_2. In addition, larger susceptibility effects due to the high magnetic field made the detection of glioma sphere xenografts even more challenging.

Tumours grown in both xenograft models were not visible on T_2-weighted images (Fig. 2a,3a, 4a, 5a and 6j) even though a ventricular enlargement indicating tumour presence was observed on the T_2-weighted image (Fig. 6) of the mouse brain with the LN-2540GS xenograft. Detection of slow-growing tumours from glioma-initiating cells was also difficult using contrast-enhanced T_1-weighted MRI (34).

During investigation of glioma sphere xenografts by means of diffusion MRI, the first evidence of tumour presence on diffusion-weighted images was revealed three months after glioma sphere cell injection for both xenograft models (Fig. 2 and Fig. 3). The absence of signs of necrosis and haemorrhagic foci in MR images, which was confirmed by histology, underlined the problematic detection of these slowly growing tumours using standard MRI techniques.

Different diffusion properties between glioma xenografts grown from LN-2669GS and LN-2540GS, respectively, were observed at three months (Table 4) and five months after cell injection (Table 5). At both time points, the larger MD in the LN-2669GS tumour model indicates that water molecules diffuse faster in tumours grown as LN-2669GS xenograft than in those grown from LN-2540GS cells that, in addition to the infiltrative part comprises a compact tumour component. Faster diffusion behaviour in the tumour grown from LN-2669GS compared to LN-2540GS is likely explained by the much lower cell density of the former (Fig. 9d, Fig. 9h). Moreover, the reduced FA in the LN-2669GS model suggests loss of anisotropy in this tumour compared to the one grown from LN-2540GS cells, indicating a looser and less anisotropic tumour microstructure in the LN-2669GS engraft, which is also in accordance with histology. However, the six gradient orientations used in this study, as described in the method

section, do not provide an optimal sampling scheme for obtaining detailed information from the FA maps.

The growth properties of the glioma sphere cell line derived xenografts in this study were highly invasive without formation of central necrosis. These properties allowed the investigation of invasive tumour characteristics which are a major diagnostic problem in patients with GBM and low grade gliomas to determine the extent of the tumour requiring treatment. Thus, our imaging results suggest that diffusion techniques can be more successful than standard T_2-weighted MR images in detecting infiltrative tumours growing slowly as xenografts in mouse brain.

The comparison between ^{1}H spectra of both the investigated xenograft models shows more pronounced changes in absolute metabolite concentrations in tumours derived from LN-2540GS than in those from LN-2669GS sphere line (Fig. 7 and Fig. 9). This may be explained by different characteristics of these tumours. Since spectra of both xenografts were measured at the same time point after cell injection (5 months), the spectral profile of tumours grown from LN-2540GS sphere line may indicate faster growing tumours compared with those grown as LN-2669GS xenograft. The diffusion results support this finding as shown by comparing MR images between both xenografts at three months (Fig. 2 and Fig. 3, respectively) and five months after cell injection (Fig. 4 and Fig. 5). Moreover, the faster growing tumours, LN-2540GS xenografts, are characterized by a lower MD compared to that of LN-2669GS xenografts. This is consistent with a more compact tumour for LN-2540GS xenograft compared to that grown from LN-2669GS sphere lines, which is in accordance with tumour histology.

Conclusion

In vivo measurements performed in this study showed that diffusion MRI technique is a useful method to detect and follow slowly growing, diffuse infiltrative tumours in the mouse brain. Imaging data in combination with localized proton spectra of lesions and immunohistochemical assessment demonstrated that the optimized diffusion MRI protocol can be useful in early detection of slow-growing human glioma xenografts as well as in the investigation of diffusion properties of tumours during their growth. Moreover, the calculated diffusion indices in the

tumours reflected microstructural differences between LN-2669GS and LN-2540GS xenografts, confirmed by histology. The diffusion parameters measured at a moderately long diffusion time (i.e. Δ = 80 ms) can be considered as potential biomarkers for early detection of diffuse infiltrative gliomas in humans due to the possible implementation of the proposed protocol on the clinical MR scanners.

Acknowledgments

We gratefully acknowledge Prof Andrew M Blamire for his helpful comments and suggestions.

We thank Dr Nicholas Kunz for his valuable advice and help during data acquisition.

This study was supported by Centre d'Imagerie BioMédicale (CIBM) of the UNIL, UNIGE, HUG, CHUV, EPFL and the Leenaards and Jeantet Foundations, and the Swiss National Science Foundation (31003A-138116 to MEH).

REFERENCES

1. Claes A, Idema AJ, Wesseling P. Diffuse glioma growth: a guerilla war. Acta Neuropathol. 2007; 114(5): 443-458.
2. Wen PY, Kesari S. Malignant gliomas in adults. N Engl J Med. 2008; 359(5): 492-507.
3. Louis DN, Perry A, Reifenberger G, von Deimling A, Figarella-Branger D, Cavenee WK, Ohgaki H, Wiestler OD, Kleihues P, Ellison DW. The 2016 World Health Organization classification of tumours of the central nervous system: a summary. Acta Neuropathol. 2016; 131(6): 803-20.
4. Stupp R, Mason WP, van den Bent MJ, Weller M, Fisher B, Taphoorn MJ, Belanger K, Brandes AA, Marosi C, Bogdahn U, Curschmann J, Janzer RC, Ludwin SK, Gorlia T, Allgeier A, Lacombe D, Cairncross JG, Eisenhauer E, Mirimanoff RO; European Organisation for Research and Treatment of Cancer Brain Tumor and Radiotherapy Groups; National Cancer Institute of Canada Clinical Trials Group. Radiotherapy plus concomitant and adjuvant termozolomide for glioblastoma. N Engl J Med. 2005; 352(10): 987-996.
5. Ceccarelli M, Barthel FP, Malta MT, Sabedot TS, Salama SR, Murray BA, Morozova O, Newton Y, Radenbaugh A, Pagnotta SM, Anjum S, Wang J, Manyam G, Zoppoli P, LingS, Rao AA, Grifford M, Cherniack AD, Zhang H, Poisson L, Carlotti CC, Tirapelli DP, Rao A, Mikkelsen T, Lau CC, Yung A, Rabadan R, Huse J, Brat DJ, Lehman LN, Barnholtz-Sloan JS, Zheng S, Hess K, Rao G, Meyerson M, Beroukhim R, Cooper L, Akbani R, Wrensch M, Haussler D, Adalpe KD, Laird PW, Gutmann DH, TCGA Research Network, Noushmehr H, Iavarone A, Verhaak RG. Molecular profiling reveals biologically discrete subsets and pathways of progression in diffuse glioma.. Cell. 2016; 164(3): 550-63.
6. Barth RF, Kaur B. Rat brain tumour models in experimental neuro-oncology: the C6, 9L, T9, RG2, F98, BT4C, RT-2 and CSN-1 gliomas. J. Neurooncol. 2009; 94(3): 299-312.

7. Huszthy PC, Daphu I, Niclou SP, Stieber D, Nigro JM, Sakariassen PØ, Miletic H, Thorsen F, Bjerkvig R. In vivo models of primary brain tumors: pitfalls and perspectives. Neuro Oncol. 2012; 14(8): 979-993.

8. Vassallo I, Zinn P, Lai M, Rajakannu P, Hamou MF, Hegi ME. WIF1 re-expression in glioblastoma inhibits migration through attenuation of non-canonical WNT signaling by downregulating the lncRNA MALAT1. Oncogene 2016; 35(1): 12-21.

9. Huse JT, Holland EC. Genetically engineered mouse models of brain cancer and the promise of preclinical testing. Brain Pathol. 2009; 19(1): 132-143.

10. Dhermain FG, Hau P, Lanfermann H, Jacobs AH, van den Bent MJ. Advanced MRI and PET imaging for assessment of treatment response in patient with gliomas. Lancet Neurol. 2010; 9: 906-920.

11. Huang RY, Neagu MR, Reardon DA, Wen PY. Pitfalls in the neuroimaging of glioblastoma in the era of antiangiogenic and immuno/targeted therapy – detecting illusive disease, defining response. Front Neurol. 2015; 6:33.

12. Porcari P, Capuani S, D'Amore E, Lecce M, La Bella A, Fasano F, Campanella R, Migneco LM, Pastore FS, Maraviglia B. In vivo (19)F MRI and (19)F MRS of (19)F-labelled boronophenylalanine-fructose complex on C6 rat glioma models to optimize boron neutron capture therapy (BNCT). Phys Med Biol. 2008; 53(23):6979-6989.

13. Padhani AR, Liu G, Koh DM, Chenevert TL, Thoeny HC, Takahara T, Dzik-Jurasz A, Ross BD, Van Cauteren M, Collins D, Hammoud DA, Rustin GJ, Taouli B, Choyke PL. Diffusion-weighted magnetic resonance imaging as a cancer biomarker: consensus and recommendations. Neoplasia 2009; 11(2): 102-125.

14. Peet AC, Arvanitis TN, Leach MO, Waldman AD. Functional imaging in adult and paediatric brain tumours. Nat Rev Clin Oncol.2012; 9(12): 700-711.

15. Price SG, Jillard JH. Imaging biomarkers of brain tumour margin and tumour invasion. Br J Radiol. 2011; Spec No 2: S159-167.

16. Durst CR, Raghavan P, Shaffrey ME, Schiff D, Lopes MB, Sheehan JP, Tustison NJ, Patrie JT, Xin W, Elias WJ, Liu KC, Helm GA, Cupino A, Wintermark M. Multimodal MR imaging model to predict tumor infiltration in patients with gliomas. Neuroradiology 2014; 56(2):107-115.

17. On N, Mitchell R, Savant SD, Bachmeier CJ, Hatch GM, Miller DW. Examination of blood-brain barrier (BBB) integrity in a mouse tumour model. J. Neurooncol. 2013; 111(2): 133-143.

18. Ganslandt O, Stadlbauer A, Fahlbusch R, Kamada K, Buslei R, Blumcke I, Moser E, Nimsky C. Proton magnetic resonance spectroscopic imaging integrated into image-guided surgery: correlation to standard magnetic resonance imaging and tumor cell density. Neurosurgery 2005;56 (Supp2) 291–298.

19. Kalpathy-Cramer I, Gerstner ER, Emblem KE, Andronesi OC, Rosen B. Advanced magnetic resonance imaging of the physical process in human glioblastoma. Cancer Res. 2014; 74(17): 4622-4637.

20. Diffusion MRI: Theory, Methods, and Applications, vol1, Jones DK (ed). Oxford: Oxford University Press 2010.

21. Wang S, Zhou J. Diffusion tensor magnetic resonance imaging of rat glioma models: a correlation study of MR imaging and histology. J. Comput. Assist. Tomogr. 2012; 36(6): 739-744.

22. Hoff BA, Chenevert TL, Bhojani MS, Kwee TC, Rehemtulla A, Le Bihan D, Ross BD, Galbán CJ. Assessment of multiexponential diffusion features as MRI cancer therapy response metrics. Magn. Reson. Med. 2010; 64(5): 1499-1509.

23. Yablonskiy DA, Sukstanskii AL. Theoretical models of the diffusion weighted MR signal. NMR Biomed. 2010; 23(7): 661-681.

24. Fieremans E, Novikov DS, Jensen JH, Helpern JA. Monte Carlo study of a two-compartment exchange model of diffusion. NMR Biomed. 2010; 23(7): 711-724.

25. Pfeuffer J, Flogel U, Dreher W, Leibfritz D. Restricted diffusion and exchange of intracellualar water: theoretical modelling and diffusion time dependence of ^{1}H NMR measurements on perfused glial cells. NMR Biomed. 1998; 11(1): 19-31.

26 Mlynárik V, Cudalbu C, Clément V, Marino D, Radovanovic I, Gruetter R. In vivo metabolic profiling of glioma-initiating cells using proton magnetic resonance spectroscopy at 14.1 Tesla. NMR Biomed. 2012; 25(4): 506-513.

27. Basser PJ. Inferring microstructural features and the physiological state of tissues from diffusion-weighted images. NMR Biomed. 1995; 8(7-8): 333-344.

28. Basser PJ, Mattiello J, Le Bihan D. MR Diffusion tensor spectroscopy and imaging. Biophys J. 1994; 259-267.

29. Basser PJ, Pierpaoli C. Microstructural and physiological features of tissues elucidated by quantitative-diffusion-tensor MRI. J. Magn. Reson. 1996; 213(2): 560-570.

30. Bennet KM, Hyde JS, Rand SD, Bennet R, Krouwer HG, Rebro KJ, Schmainda KM. Intravoxel distribution of DWI decay rates reveals C6 glioma invasion in rat brain. Magn. Reson. Med. 2004; 52(5): 994-1004.

31. Lope-Piedrafita S, Garcia-Martin ML, Galons JP, Gillies RJ, Trouard TP. Longitudinal diffusion tensor imaging in a rat brain glioma model. NMR Biomed. 2008; 21(8): 799-808.

32. Maier SE, Sun Y, Mulkern RV. Diffusion imaging of brain tumors. NMR Biomed. 2010; 23(7): 849-864.

33. Kallenberg K, Goldmann T, Menke J, Strik H, Bock HC, Stockhammer F, Buhk JH, Frahm J, Dechent P, Knauth M. Glioma infiltratation of corpus callosum: early signs detected by DTI. J. Neurooncol. 2013; 112(2): 217-222.

34. Painter KJ, Hillen T. Mathematical modelling of glioma growth: the use of diffusion tensor imaging (DTI) data to predict the anisotropic pathways of cancer invasion. J. Theor Biol. 2013; 323: 25-39.

35. Sciuscio D, Diserenc AC, van Dommelem K, Martinet D, Jones G, Janzer RC, Pollo C, Hamou MF, Kaina B, Stupp R, Levivier M, Hegi ME. Extent and patterns of MGMT promoter methylation in glioblastoma- and respective glioblastoma-derived spheres. Clin Cancer Res. 2011; 17(2): 255-266.

36. Bady P, Diserens AC, Castlella V, Kalt S, Heinimann K, Hamou MF, Delorenzi M, Hegi ME. DNA fingerprinting of glioma cell lines and considerations on similarity measurements. Neuro Oncol. 2012; 14(6): 701-711.

37. Gruetter R, Tkáč I. Field mapping without reference scan using asymmetric echo-planar techniques. Magn Reson Med. 2000; 43(2): 319-323.

38. Tanner JE. Use of stimulated-echo in NMR diffusion studies. J Chem Phys. 1970; 52; 2523-2526.

39. Mlynárik V, Gambarota G, Frenkel H, Gruetter R. Localized short-echo-time proton MR spectroscopy with full signal-intensity acquisition. Magn Reson Med. 2006; 54(5): 965-970.

40. Tkáč I, Starčuk Z, Choi IY, Gruetter R. In vivo 1H NMR spectroscopy of rat brain at 1ms echo time. Magn Reson Med. 1999; 41(4): 649-656.

41. Provencher SW. Estimation of metabolite concentrations from localized in vivo proton NMR spectra. Magn Reson Med. 1993; 30(6): 672-679.

42. Nair G, Tanahashi Y, Low HP, Billings-Gagliardi S, Schwartz WJ, Duong TQ. Myelination and long diffusion times alter diffusion-tensor-imaging contrast in myelin-deficient shiverer mice. Neuroimage 2005; 28(1): 165-174.

Table 1. DWI protocol used to optimize tumour visualization.
Summary of diffusion gradient amplitudes (*G*) corresponding to each *b* value and diffusion time (Δ) used in the DWI acquisition.

b values [s/mm^2]	*G* [G/cm]					
	Δ = 40ms	Δ = 60ms	Δ = 80ms	Δ = 100ms	Δ = 150ms	Δ = 220ms
294	4.6	2.0	0.0	-	-	-
389	6.0	3.6	1.8	0.2	-	-
542	7.8	5.4	3.6	2.3	-	-
754	9.7	7.3	5.4	4.1	1.6	-
1024	11.9	9.4	7.2	5.9	3.5	1.3
1352	14.0	11.4	9.0	7.5	4.6	2.4
2185	19.1	15.8	12.6	10.4	7.8	5.0
2688	21.3	17.4	14.4	12.2	9.0	5.8

A missing value (-) means *b*0 value higher than the considered *b*-values (*b*0 = 381, 590 and 884 s/mm^2 for Δ = 100, 150 and 220ms, respectively).

Table 2. Summary of CNR determined from DW images acquired with different Δ and *b*-values from mouse brain with slow growing and highly infiltrative tumour at early stage of growth.

b values [s/mm^2]	CNR					
	Δ = 40ms	Δ = 60ms	Δ = 80ms	Δ = 100ms	Δ = 150ms	Δ = 220ms
294	-0.43 ± 0.08	0.16 ± 0.04	0.54 ± 0.10	-	-	-
389	0.53 ± 0.02	0.87 ± 0.04	1.01 ± 0.15	0.88 ± 0.09	-	-
542	0.52 ± 0.04	0.94 ± 0.12	1.61 ± 0.08	1.46 ± 0.12	-	-
752	1.22 ± 0.07	1.44 ± 0.09	1.63 ± 0.09	1.66 ± 0.06	1.44 ± 0.04	-
1024	1.34 ± 0.09	1.72 ± 0.06	2.05 ± 0.07	1.89 ± 0.05	1.55 ± 0.08	1.31 ± 0.08
1352	1.51 ± 0.12	1.84 ± 0.10	2.36 ± 0.12	2.04 ± 0.11	1.83 ± 0.13	1.47 ± 0.12
2185	0.98 ± 0.09	1.43 ± 0.09	1.98 ± 0.10	1.24 ± 0.23	1.01 ± 0.09	0.86 ± 0.25
2688	0.71 ± 0.10	1.01 ± 0.08	1.44 ± 0.09	0.80 ± 0.16	0.37 ± 0.09	-0.16 ± 0.03

All values are (mean ± SD).
A missing value (-) indicates no DW images available for the evaluation of the CNR.

Table 3. Summary of *ADC* values, FA and MD indices of tumour (T) and contralateral (CL) area of both LN-2669GS and LN-2540GS xenografts at early stages of tumour development (3 months after cell injection).
ADC values and DTI indices obtained from the corresponding brain regions of the control group are also reported. Data are mean ± 1 s.e.m.

	LN-2669GS xenograft		LN-2540GS xenograft		Control*
	T	CL	T	CL	
ADC $[10^{-3}mm^2/s]$	0.65 ± 0.04$^{¶¥}$	0.53 ± 0.06	0.64 ± 0.02$^{¶¥}$	0.54 ± 0.05	0.56 ± 0.02
FA	0.15 ± 0.03$^{\#}$	0.18 ± 0.04	0.19 ± 0.03	0.18 ± 0.03	0.18 ± 0.05
MD $[10^{-3}mm^2/s]$	0.69 ± 0.07$^{¶¥\#}$	0.58 ± 0.05	0.64 ± 0.05$^{¶¥}$	0.58 ± 0.03	0.58 ± 0.03

* Control data were computed from regions corresponding to tumour location, symmetrically in both hemispheres. Statistics: ¶ significantly different from CL area in the same group (paired two-tailed t test, $p < 0.01$); $^{¥}$ significantly different from the related brain regions in the controls (unpaired two-tailed t test, $p<0.01$), $^{\#}$ significantly different from the corresponding value in tumour grown as LN-2540GS xenograft.

Table 4. Summary of *ADC* values, FA and MD indices of tumour (T) and contralateral (CL) area of both LN-2669GS and LN-2540GS xenografts at 5 months after cell injection.
ADC values and DTI indices obtained from the corresponding brain regions of the control group are also reported. Data are mean ± 1 s.e.m.

	LN-2669GS xenograft		LN-2540GS xenograft		Control*
	T	CL	T	CL	
ADC [$10^{-3}mm^2/s$]	0.67 ± 0.07$^{¶¥}$	0.53 ± 0.07	0.65 ± 0.04$^{¶¥}$	0.54 ± 0.05	0.54 ± 0.02
FA	0.16 ± 0.02$^{#¶¥}$	0.19 ± 0.02	0.20 ± 0.03	0.19 ± 0.02	0.19 ± 0.02
MD [$10^{-3}mm^2/s$]	0.71 ± 0.04$^{#¶¥}$	0.57 ± 0.04	0.66 ± 0.05$^{¶¥}$	0.56 ± 0.03	0.57 ± 0.03

* Control data were computed from regions corresponding to tumour location, symmetrically in both hemispheres. Statistics: ¶ significantly different from CL area in the same group (paired two-tailed t test, $p < 0.01$); ¥ significantly different from the related brain regions in the controls (unpaired two-tailed t test, $p<0.01$), # significantly different from the corresponding value in tumour grown as LN-2540GS xenograft.

Figure Captions

Figure 1. *In vivo* MRI of LN-2540GS glioma sphere xenograft, 80 days after cell injection (pilot study data). Diffusion-weighted images of a mouse brain with LN-2540GS glioma sphere xenograft acquired with different diffusion times (Δ = 40, 60, 80, 100, 150, 220 ms) and same *b*-value (1352 s/mm^2). Image (c) shows a slightly better tumour contrast compared to others.

Figure 2. *In vivo* MRI of LN-2669GS glioma sphere xenograft, three months after cell injection. Upper panel: coronal T_2-weighted (a) and diffusion-weighted (b) images of the mouse brain with LN-2669GS xenograft NCH-1364, and the calculated ADC (c) map. Lower panel: corresponding diffusion tensor maps, MD (d), FA (e) and FA-modulated directionally encoded colour DEC (f) maps. The lesion (arrow) is barely visible on the diffusion-weighted image (b), ADC (c) and DTI maps.

Figure 3. *In vivo* MRI of LN-2540GS glioma sphere xenograft, three months after injection of the cells. Upper panel: coronal T_2-weighted (a) and diffusion-weighted (b) images of the mouse brain with LN-2540GS xenograft NCH-1365, and the calculated ADC (c) map. Lower panel: corresponding diffusion tensor maps, MD (d), FA (e) and FA-modulated DEC (f) maps. The lesion (arrow) is visible on the diffusion-weighted image (b), ADC (c) and DTI maps.

Figure 4. *In vivo* MRI of LN-2669GS glioma sphere xenograft, five months after injection of the cells. Upper panel: coronal T_2-weighted (a) and diffusion-weighted (b) images of the mouse brain with LN-2669GS xenograft NCH-1364, and the calculated ADC (c) map. Lower panel: corresponding diffusion tensor maps, MD (d), FA (e) and FA-modulated DEC (f) maps. Lesion (arrow) is visible on the diffusion-weighted image (b), ADC (c) and DTI maps. Due to the highly invasive and diffuse character of this tumour (corresponding histology, Fig. 10) it is difficult to delineate tumour borders.

Figure 5. *In vivo* MRI of LN-2540GS glioma sphere xenograft, five months after injection of the cells. T_2-weighted (a) and diffusion-weighted (b) images, MD (b), FA (c) and FA-modulated DEC maps of a coronal slice from the mouse brain with the LN-2540GS xenograft NCH-1365.

MD, FA and DEC maps, computed after DTI reconstruction, show a lesion (indicated by arrow).

Figure 6. *In vivo* MRI of LN-2540GS glioma sphere xenograft (A) and CNR data of both xenografts (B), all acquired during the last MRI session (five months after injection of the cells).
(A) Left panel: coronal diffusion-weighted images (a – h) of the mouse brain with LN-2540GS xenograft NCH-1365. Images are related to the DWI acquisition with *b*-values increasing along the read-out direction. Right panel: corresponding anatomical T_2-weighted image (j) and ADC map (h) of glioma-bearing xenograft. Images were acquired 15 days after those shown in Fig. 5. Lesion (indicated by arrow and delineated by a dotted line in (g)) is visible on the diffusion-weighted images (c – h) and the ADC map.
(B) The CNR data of LN-2669GS xenograft NCH-1364 and LN-2540GS xenograft NCH-1365 as function of *b*-values obtained in the last MRI session.

Figure 7. ^{1}H spectra of the brain from a control mouse (a) and from a tumour derived from LN–2669GS, xenograft NCH-1364 (b) and a tumour derived from LN–2540GS, xenograft NCH-1365 (c). Spectrum (b) and (c) were acquired 5 months after cells injection. Spectra were displayed with a Gaussian filter (0.11).

Figure 8. Absolute metabolite concentrations in the tumours grown from LN-2669GS and LN-2450GS sphere lines as well as in the same brain region of control obtained by in vivo MR spectroscopy at five months after injection of the cells.
Statistic: * absolute metabolite concentrations from tumour grown from LN-2669GS NCH-1364 significantly different from those of the same brain region of controls ($p < 0.05$; **, $p < 0.01$; ***, $p < 0.001$; ****, $p < 0.0001$); ††† absolute metabolite concentrations from tumour grown from LN-2540GS NCH-1365 significantly different from those of the same brain region of controls ($p < 0.001$; ††††, $p < 0.0001$).

Figure 9. Histology of the LN-2669GS and LN-2540GS derived xenografts. For both xenografts full brain sections are shown for haematoxylin and eosin stain (H&E) (a, e), and

immunohistochemistry for the glial fibrillary acidic protein (GFAP) (b, f), and the human specific nucleolin protein (NCL) (c, d, g, h).

(A) In the LN-2669GS xenograft (NCH-1364), the H&E stained section (a) does not reveal the lesion with the exception of a small compact tumour part at the surface of the brain due to reflux at the injection site. The GFAP (b) expression (arrow) indicates gliosis induced by infiltrating tumour cells. The visualization of the human tumour cells by hNCL (c, d) indicates the highly invasive growth properties of the LN-2669GS xenograft NCH-1364 (magnification of the marked area (*), scale bar 10 μm).

(B) The LN-2540GS xenograft is readily visible by H&E, identifying a compact and an invasive part (e). Magnification of the marked area (*) in the hNCL immunostained section (h) indicates high cell density in the most compact part of the LN-2540GS xenograft NCH-1365 (scale bar 10 μm).

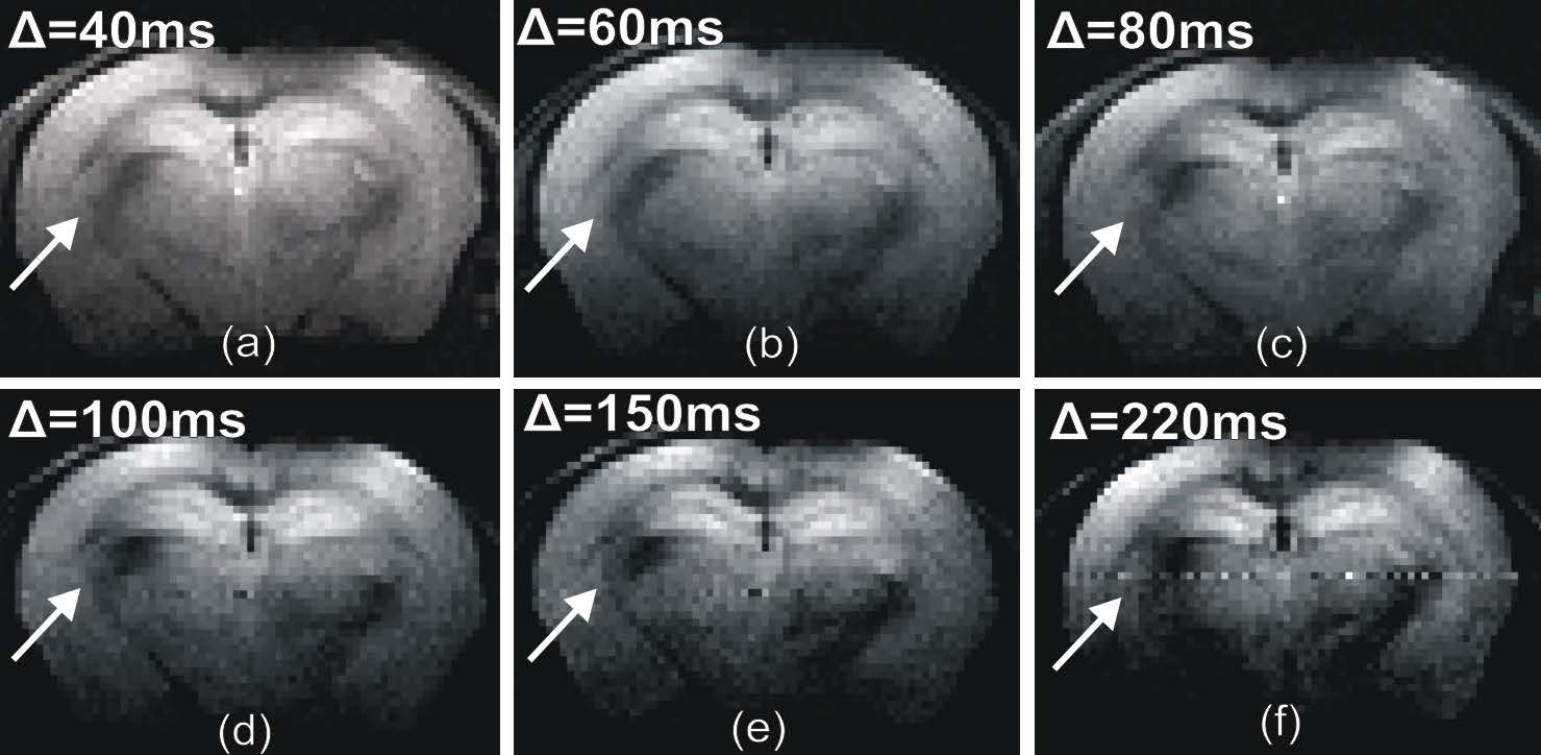
Δ=40ms
(a)
Δ=60ms
(b)
Δ=80ms
(c)
Δ=100ms
(d)
Δ=150ms
(e)
Δ=220ms
(f)

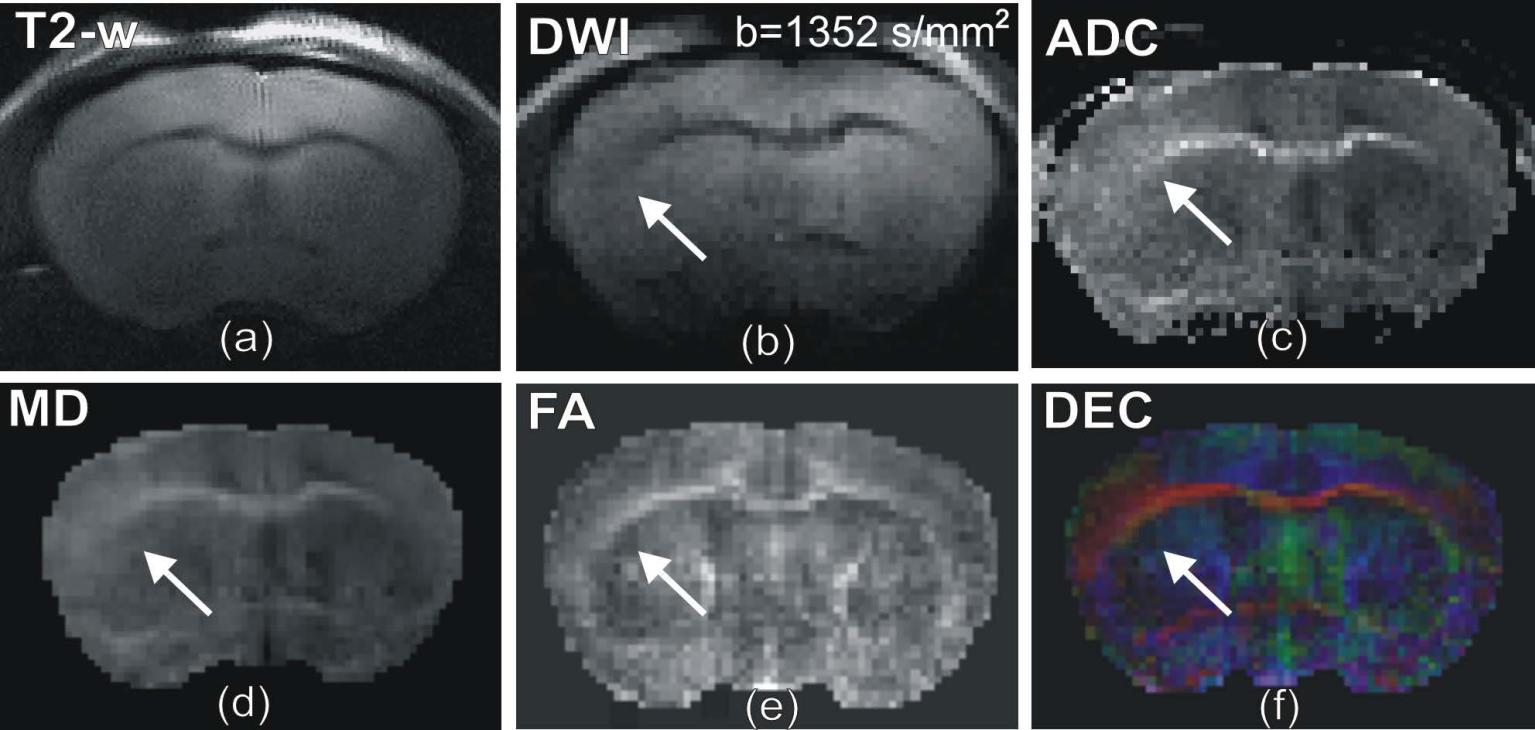
T2-w
(a)
DWI
b=1352 s/mm2
(b)
ADC
(c)
MD
(d)
FA
(e)
DEC
(f)

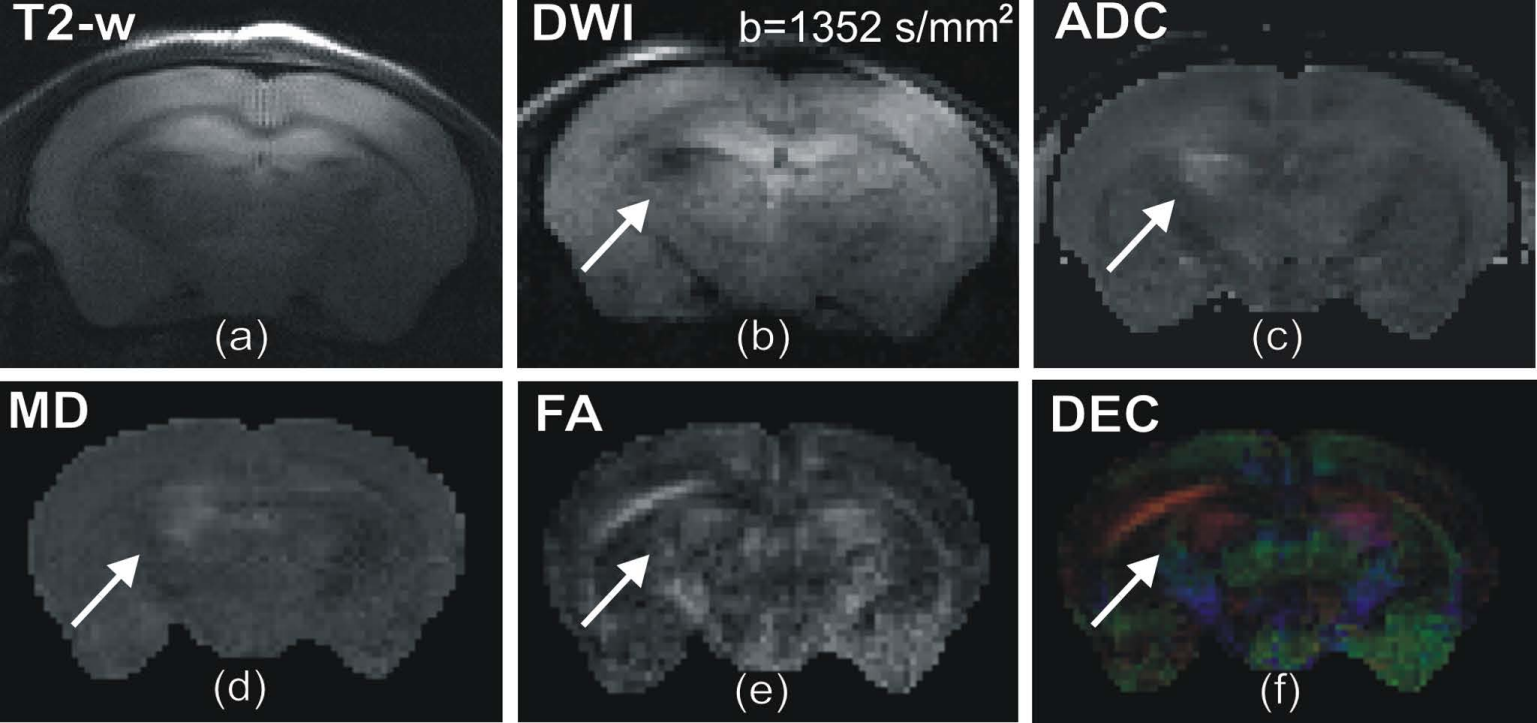
T2-w
(a)
DWI
b=1352 s/mm²
(b)
ADC
(c)
MD
(d)
FA
(e)
DEC
(f)

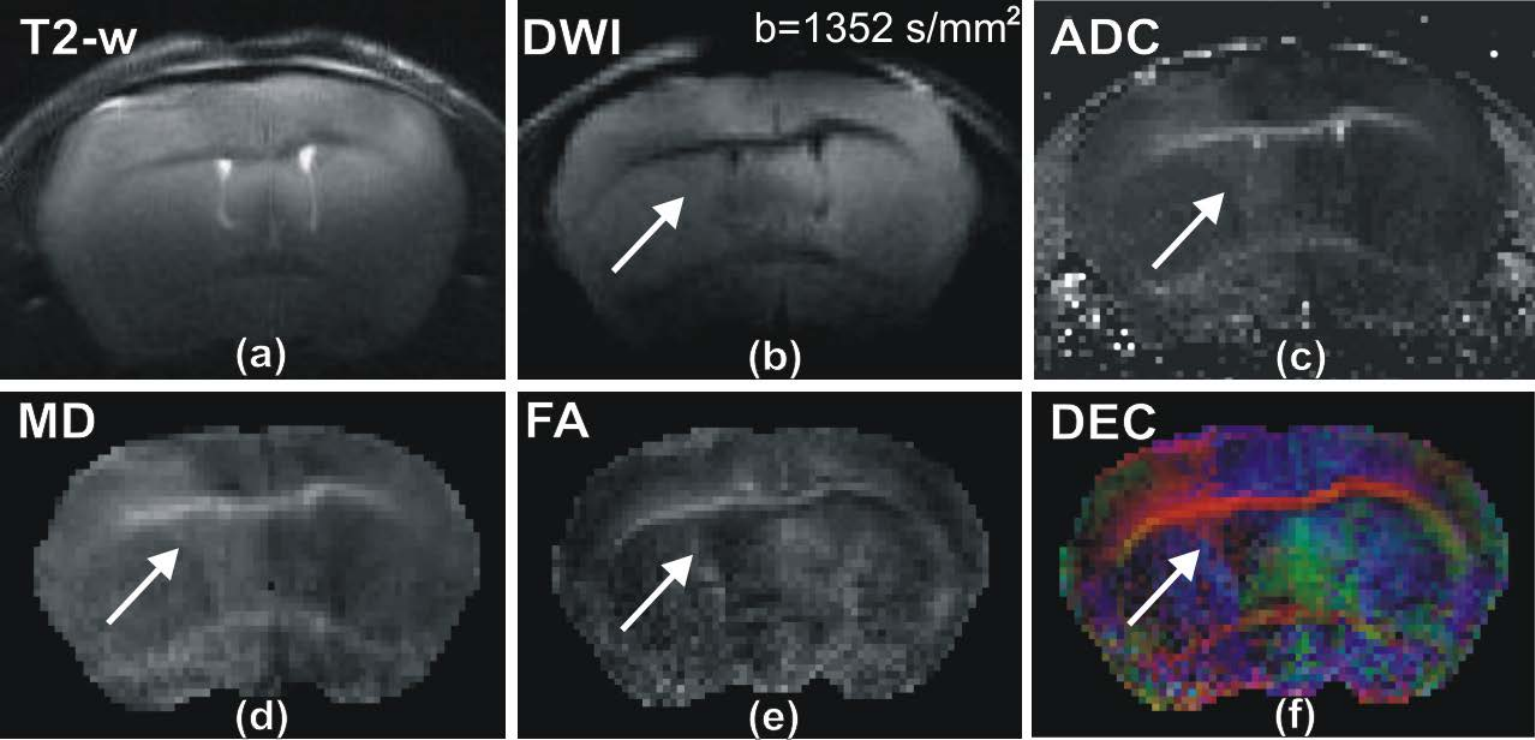
T2-w
DWI
b=1352 s/mm2
ADC
(a)
(b)
(c)
MD
FA
DEC
(d)
(e)
(f)

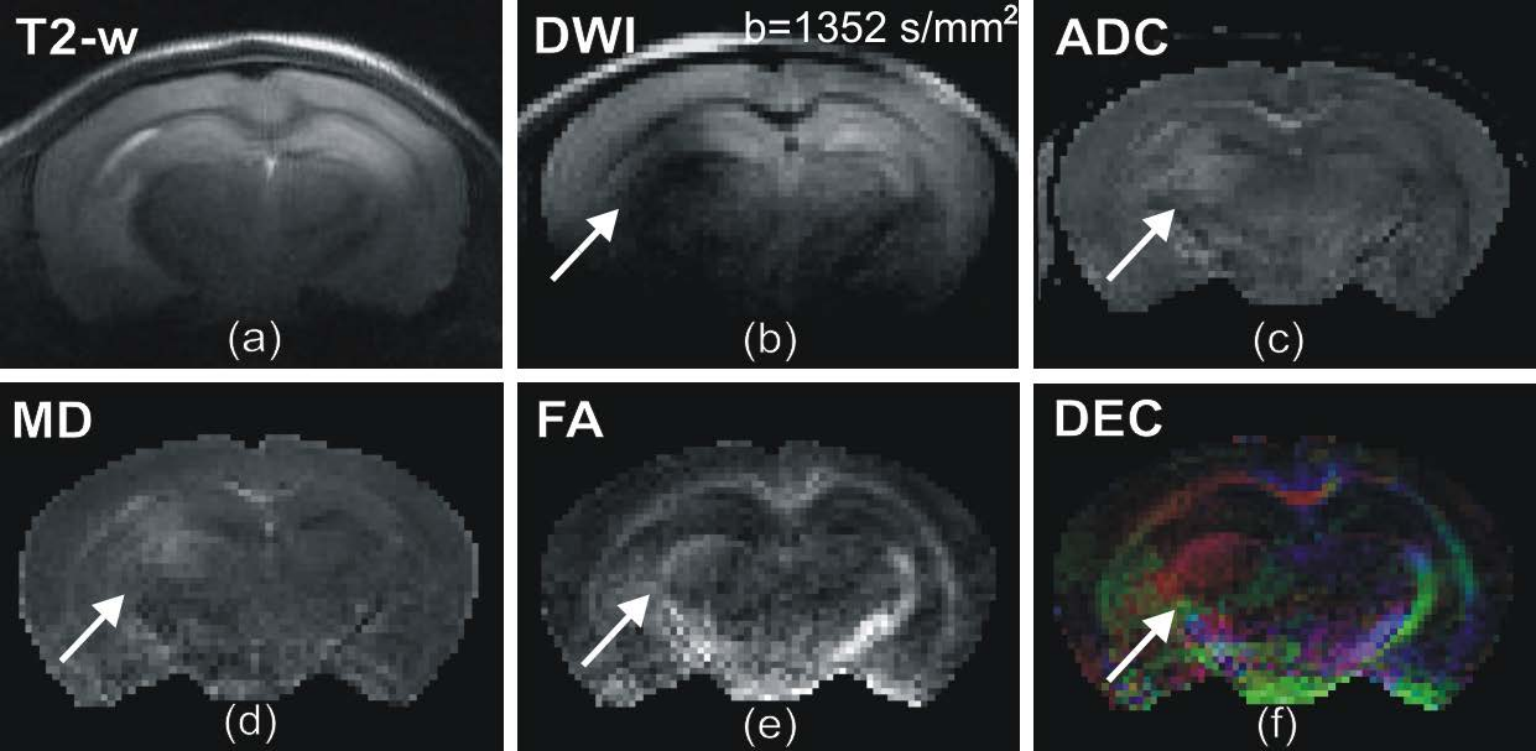
T2-w
(a)
DWI
b=1352 s/mm2
(b)
ADC
(c)
MD
(d)
FA
(e)
DEC
(f)

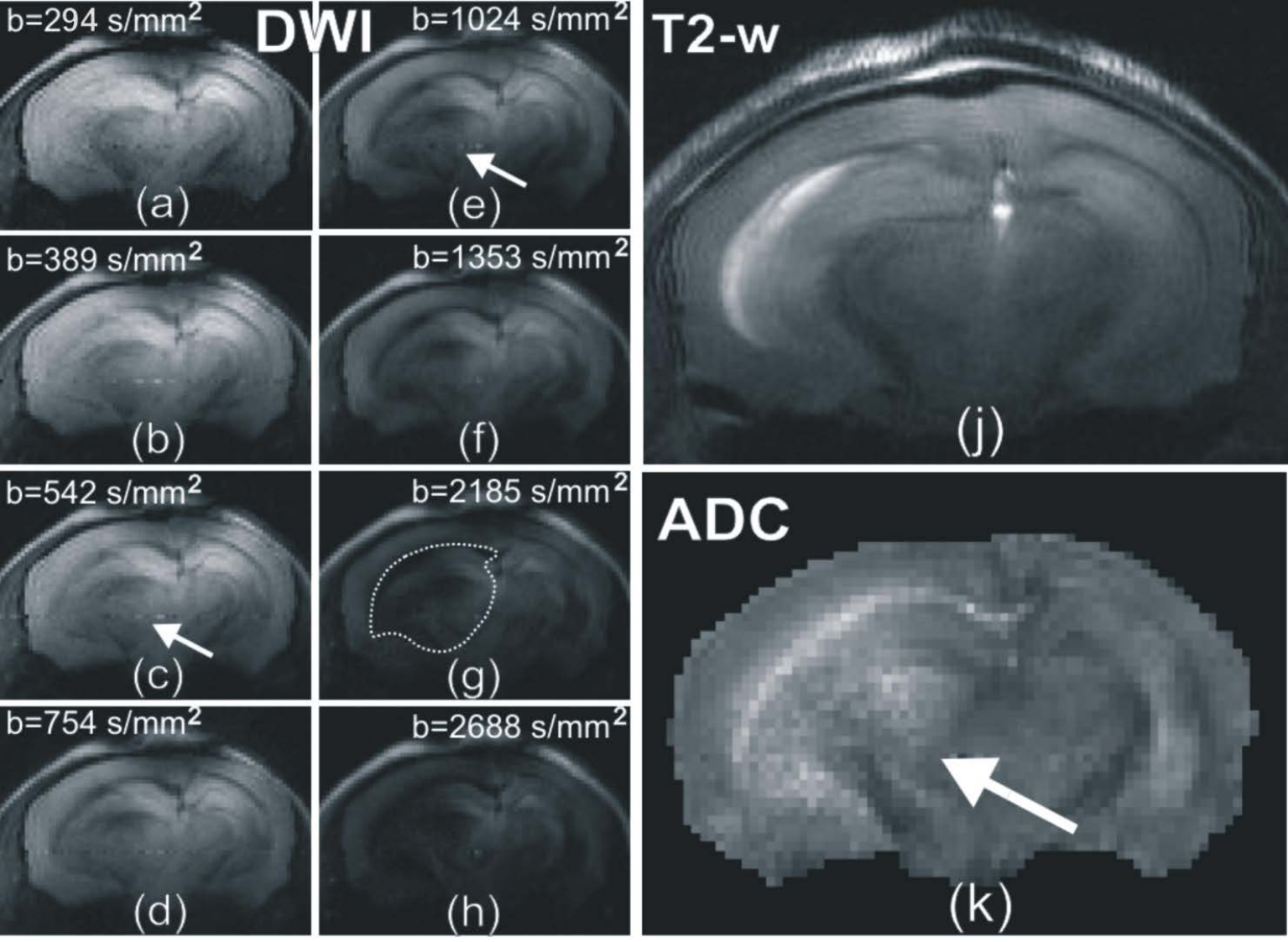
b=294 s/mm2
DWI
b=1024 s/mm2
T2-w
(a)
(e)
(j)
b=389 s/mm2
b=1353 s/mm2
(b)
(f)
b=542 s/mm2
b=2185 s/mm2
ADC
(c)
(g)
(k)
b=754 s/mm2
b=2688 s/mm2
(d)
(h)

A

B

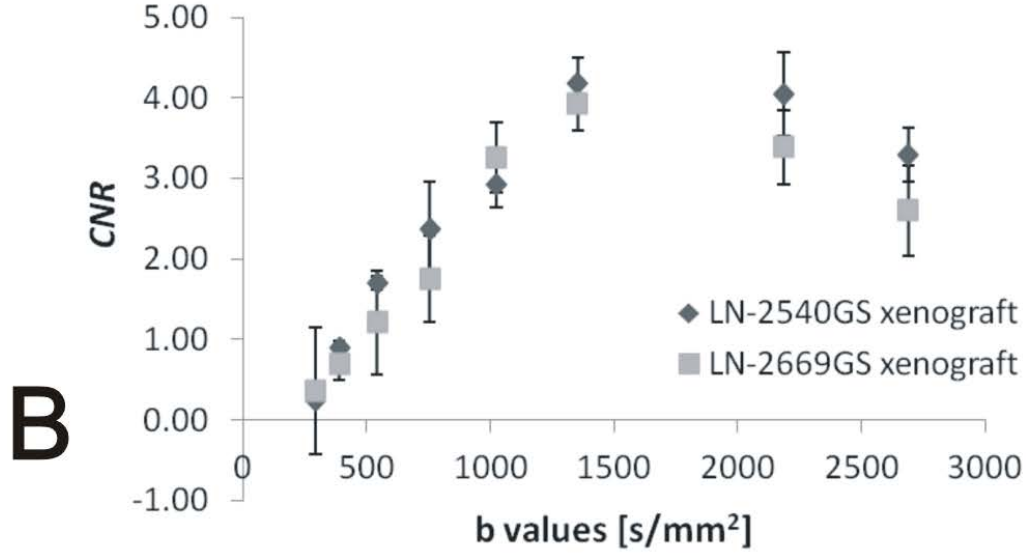
5.00
4.00
3.00
2.00
1.00
0.00
-1.00
CNR
0
500
1000
1500
2000
2500
3000
b values [s/mm2]
LN-2540GS xenograft
LN-2669GS xenograft

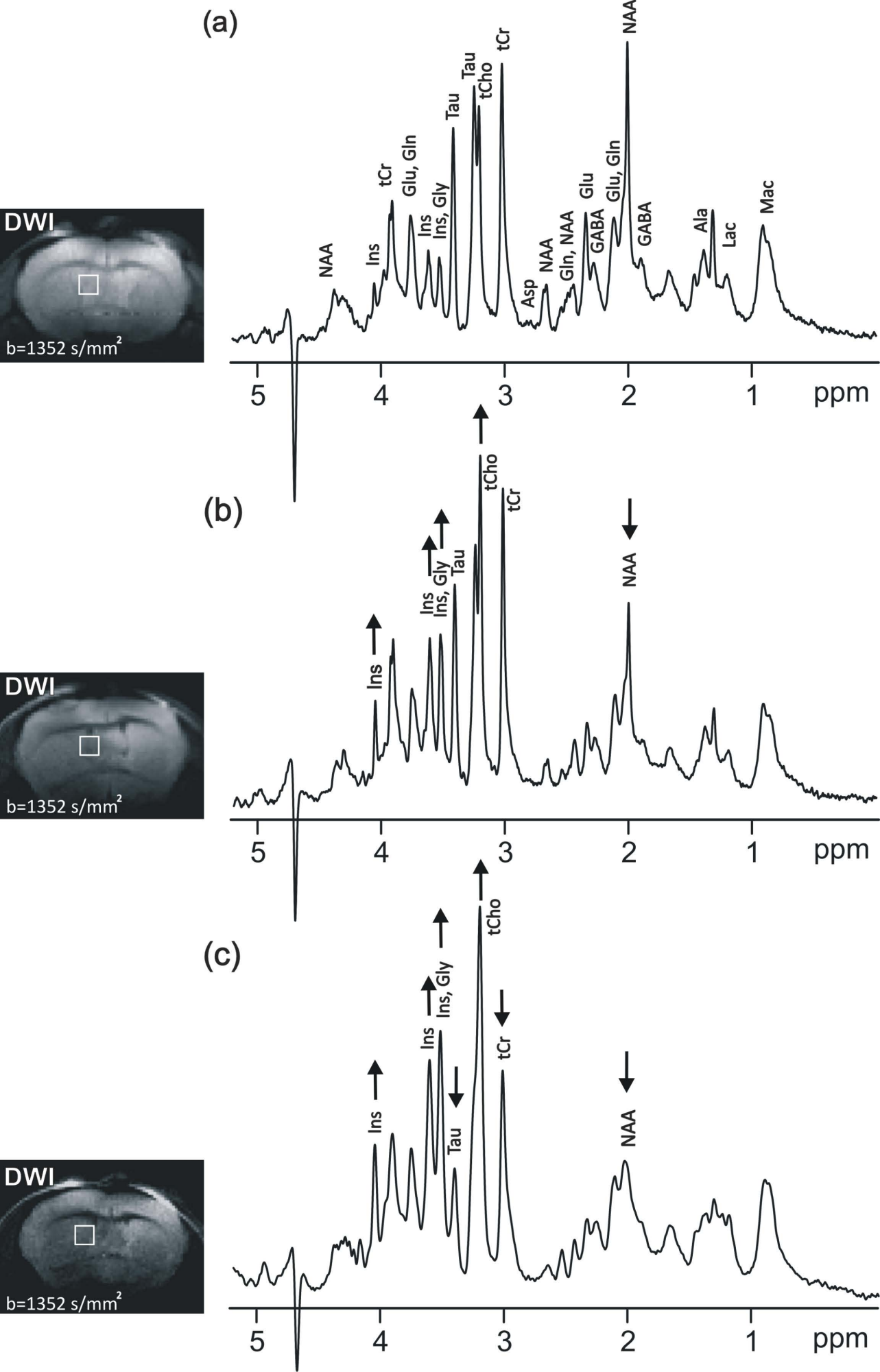
(a)
DWI
b=1352 s/mm²
NAA
Ins
tCr
Glu, Gln
Ins
Ins, Gly
Tau
Tau
tCho
tCr
Asp
NAA
Gln, NAA
Glu
GABA
Glu, Gln
NAA
GABA
Ala
Lac
Mac
5
4
3
2
1
ppm
(b)
DWI
b=1352 s/mm²
Ins
Ins
Ins, Gly
Gly
Tau
tCho
tCr
NAA
5
4
3
2
1
ppm
(c)
DWI
b=1352 s/mm²
Ins
Ins
Ins, Gly
Tau
tCho
tCr
NAA
5
4
3
2
1
ppm

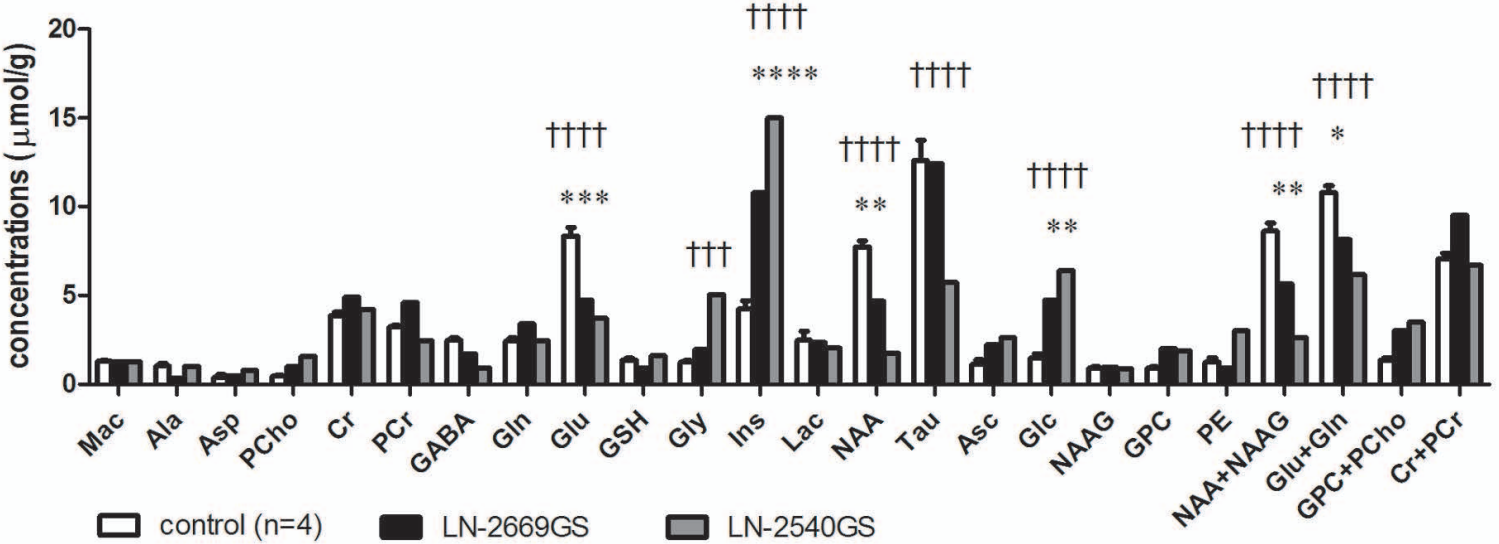
concentrations (μmol/g)
20
15
10
5
0
Mac
Ala
Asp
PCho
Cr
PCr
GABA
Gln
Glu
GSH
Gly
Ins
Lac
NAA
Tau
Asc
Glc
NAAG
GPC
PE
NAA+NAAG
Glu+Gln
GPC+PCho
Cr+PCr
†††† ***
†††
†††† ****
†††† **
††††
†††† **
†††† **
†††† *
control (n=4)
LN-2669GS
LN-2540GS

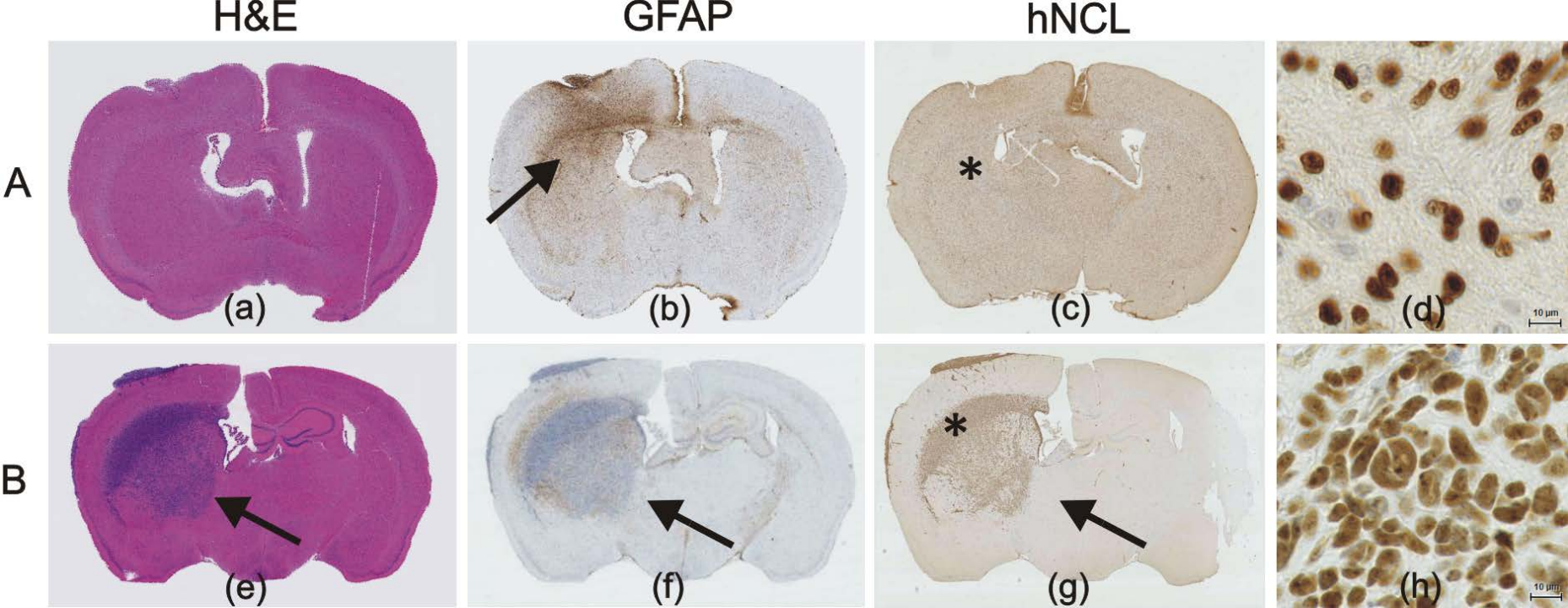
H&E
GFAP
hNCL
A
B
(a)
(b)
(c)
(d)
(e)
(f)
(g)
(h)
10 µm
10 µm